Rock permittivity characterization and application of electromagnetic mixing models for density/compactness assessment of HMA by means of step-frequency radar

Steven Araujo, Laurent Delbreilh, Laurent Laguerre, Hervé Dumont, Eric Dargent, Cyrille Fauchard

Rock permittivity characterization and application of electromagnetic mixing models for density/compactness assessment of HMA by means of Step Frequency Radar.

Steven Araujo[a,b], Laurent Delbreilh[b], Laurent Laguerre[c], Hervé Dumont[d], Éric Dargent[b], Cyrille Fauchard[a,b,*]

[a]*Cerema, Direction Territoriale Normandie Centre, 10 chemin de la poudrière - CS 90245 - F-76121, Le Grand-Quevilly Cedex, France.*
[b]*AMME-LECAP EA 4528 International Lab., Av. de l'Université, Normandie Université France, Université de Rouen, BP12, 76801, Saint-Étienne-du-Rouvray, France*
[c]*Ifsttar, LUNAM Université, Route de Bouaye, CS4, 44344 Bouguenais Cedex, France.*
[d]*Eiffage Travaux Publics, 3-7 place de l'Europe, 78140 Vélizy-Villacoublay, France.*

Abstract

This work aims to determine the compactness/density of Hot Mix Asphalt (HMA) by measuring its permittivity by means of Step Frequency Radar (SFR). As HMA is mainly made of rocks, their dielectric properties are measured in the frequency range applied with SFR [0.5-4 GHz] using cylindrical cavities. The results show that the rocks can be considered as lowloss dielectric. As electromagnetic mixing models are required to switch from the measured permittivity to the compactness, Power Law (PL) models and Unified Mixing Rules (UMR) are applied to laboratory experiment. Slabs permittivity of various compactness are determined with the help of the SFR system. This study shows that (i) the selection of the electromagnetic mixing model has a critical impact on the accuracy of the calculated compactness, (ii) the choice of the host matrix for UMR family has huge consequences and (iii) the best assessment of compactness/density is given by CRIM, Rayleigh and Böttcher models with aggregate matrix.

Keywords: Permittivity, GPR, density, compactness, Step Frequency Radar, electromagnetic mixing model.

1. Introduction

The dielectric characterization of rocks is of great interest for exploration in geophysics. The electromagnetic (EM) methods for soil prospection require a good comprehension of EM waves interaction with soil, as well as an accurate knowledge of the dielectric properties of the observed materials. Dielectric measurements can help in various areas such as volcanic rock study (Gomaa and Elsayed, 2009), estimation of rock porosity in petrolum reservoirs (Tong and Tao, 2008), new methods for oil shale extraction (Lopatin and Martemyanov, 2012), rock wettability and grain size, water and clay influences in soil (Bona et al., 2002; Dobson et al., 1985; Hallikainen et al., 1985; Lesmes and Morgan, 2001), water-bearing rocks (Chelidze and Gueguen, 1999; Chelidze et al., 1999) or dry geological materials (Saint-Amant and Strangway, 1970). In civil engineering, the widespread use of Ground Penetrating Radar (GPR)

*Corresponding author
Email address: cyrille.fauchard@cerema.fr, Tel. +33235689295, Fax +33235688188 (Cyrille Fauchard)

methods for non-destructive purposes (Al-Qadi and Lahouar, 2004; Benedetto and Tosti, 2013) has led to the study of man-made materials dielectric properties. Robert (1998) studied the dielectric behaviour of concrete between 50 MHz and 1 GHz. Maierhofer and Wöstmann (1998) assessed the dielectric properties of brick materials and porous concrete as a function of moisture and salt content at 7 GHz. Hasar (2009) measured the hardened mortar and cement with various water-content in the frequency band [8-12 GHz].

For dry civil engineering materials such as HMA, the rock proportion generally represents as much as 88 to 96 % of the mix. Hence the knowledge of the rock dielectric properties is of major importance and represents a consistent a-priori information for thickness or density controls performed on site with GPR or SFR systems. As a matter of fact, the dielectric characterization of dry rocks has already been undertaken but for different purposes: Ulaby et al. (1990) in support of radar investigation to Mars, studied 80 samples of igneous and sedimentary rocks in the microwave region [0.5-18 GHz]. Campbell and Ulrichs (1969) conducted similar measurements on lunar samples at 450 MHz and 35 GHz.

In the first section of this work, the complex permittivity of 24 magmatic, sedimentary and metamorphic rocks are measured in cylindrical cavities at 6 frequencies in the microwave region. They have mainly been extracted from quarries providing road manufacturers in building materials. These measurements complete a previous study carried out on 11 rock types (Fauchard et al., 2013) and a discussion is proposed on the measured values and their dependency to the rock bulk density and their mineral composition.

The HMA density (and its equivalent compactness, or indice of compaction) is one of the key parameters to control for the reception of newly-paved roads. Nuclear tests based on gamma ray interaction with matter (ASTM D2950 / D2950M, 2011; ASTM D6938 - 10, 2010) can be implemented directly on site and have been considered since the 70's as the only non-destructive method for assessing in-place density. Nevertheless, nuclear methods tend to disappear because of the cost induced by their transportation and storage. Their radiations also threaten the life users. Nowadays, core testing in the lab remains the only reference method valuable for density evaluation. Two main core methods are suitable and standard: the paraffin coated test samples (NF EN 12697-6, 2012) and the nuclear bench (NF EN 12697-7, 2003). The challenge to take up today is to develop non-destructive on site testing, without the constraints of nuclear devices. SFR system allows getting the HMA permittivity which is relied to the density by electromagnetic models. In that purpose, the basic principle of mixing rules are mainly taken from the work of Sihvola (1999) and the results are widely compared with Al-Qadi et al. (2010), Leng et al. (2011) and Fauchard et al. (2015). In the second section of this work, these models are applied and discussed to a laboratory investigation.

2. Rock permittivity measurements

2.1. Lab experiments and results

As a HMA mainly consists of 88% to 96% of rocks, the dielectric characterization of rocks is a major issue for the comprehension of HMA electromagnetic behaviour. Hence, the knowledge of dielectric properties of rocks in

the frequency band used in civil engineering application has been undertaken. This study updates some results of a previous work (Fauchard et al., 2013) and intends to test dielectric mixture models selected in the litterature. In order to evaluate the HMA density with radar methods, rocks extracted from various quarries for road manufacturing have been studied. The table 1 reports the name, the measurement date (2013 and 2015), the origin and the rock feature. Furthermore, other rocks that are not used for road manufacturing such as the volcanic basalt of the Piton de la Fournaise, or the limestone from Caen, are reported for knowledge purpose.

A portable network analyser (PNA, Agilent E8362B) and two cylindrical cavities (ϕ=400 mm and ϕ=200 mm) allow the complex permittivity measurement of 4-5 cm-diameter and 2.52 cm-height cylindrical rock samples at six frequencies (0.57 GHz, 1.32 GHz, 2.06 GHz and 1.15 GHz, 2.63 GHz and 4.13 GHz, respectively). A previous study carried out on 11 different rocks has reported the good repetability of this method (Fauchard et al., 2013). Indeed, the permittivity of each tested rocks was averaged on 10 to 15 cores for one single type of rock at six frequencies. However a substantial heterogeneity were observed in a given set of cores extracted from a single vein. In this study, 24 rocks are tested, including the aformentioned rocks. Herein, just one cylindrical core by rock type is extracted and measured twice (side and upside down) at six frequencies. Hence, the standard deviation of the 2015 measurements is calculated from 12 permittivity values. The purpose is to record a high frequency reference permittivity that will be used for further works in the low frequency domain. Rocks were dried 48h at 115°C in oven before measurement. The real ($\epsilon_r^{'}$) and imaginary dielectric ($\epsilon_r^{"}$) constants, the loss tangent ($tan\delta$) and the density (ρ [1]) are reported in the table 1. The real and imaginary part of the permittivity and the loss tangent are respectively shown in the Fig.1(a), 1(b) and 1(c).

2.2. Discussion on the measured permittivity

The real dielectric permittivity ranges from 4 to 9 and these results are in accordance with the studies of Ulaby et al. (1990) and Parkhomenko (1967). There is no significant evidence of the values distribution of permittivity as a function of rock formation (sedimentary, magmatic of metamorphic). The imaginary part of the permittivity exhibits strong standard deviation related, first, to the experimental system, and second, to the losses. According to Li et al. (1981), cylindrical cavity allows an accuracy of 1% on the real part of the permittivity and 2% for the imaginary part. This uncertainty may increase respectively from 1% to 2% and from 2% to 5% by taking into account the uncertainty measurement of sample dimensions. The measurements highlight a slight dispersion on the real part of the permittivity which is negligible over the 6 used frequencies (less than 1%). However, a stronger dispersion is noticeable on the imaginary part. First, this could be due to water molecules which were not evaporated during the annealing (115°C for 48h). This water (probably bounded) induces an interfacial polarization (Maxwell-Wagner-Sillar) ((Benedetto, 2010; Kaden et al., 2013; Saltas et al., 2008)) which is basically observable about 0.5 to 1 GHz and at lower frequencies as well. Second, another phenomenon such as interfacial polarization between mineral structures should also be

[1] For rocks, the relative density ρ/ρ_{water} is named density with $\rho_{water} = 1g/cm^3$ at $4°C$

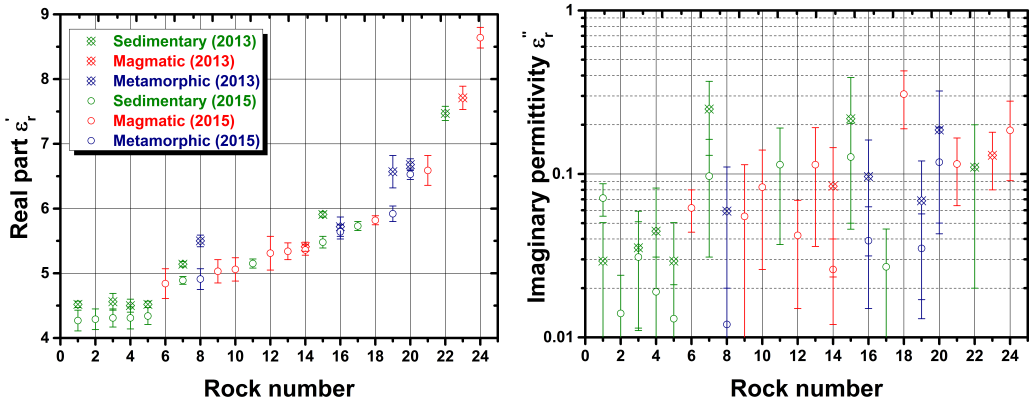

(a) Real part of the permittivity

(b) Imaginary part of the permittivity

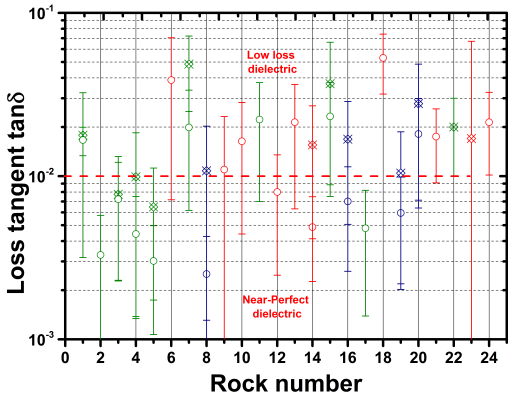

(c) Loss tangent

Figure 1: Dielectric characterization of 24 rocks obtained by means of cylindrical cavities at 0.57 GHz, 1 GHz, 1.7 GHz, 1.15 GHz, 2.63 GHz and 4.13 GHz. Rock details are given in the table 1.

considered and will be undertaken in the future through petrographic and chemical studies. By covering the frequency band from 0.5 to 4 GHz, relaxation phenomena may occur and might explain such high dispersion. However, despite the variation of the imaginary part, the loss tangent ranges between 0.1 to 0.01, in such a manner that tested rocks can be considered as low-loss dielectrics.

Overall, the differences betweeen the 2013 and 2015 measurements are about 0.2 for the real part of the permittivity which is close to the standard deviation of the measurement for a given rock. However four of them (rhyolite, gneiss, quartz arenite and amphibolite) highlight a higher difference probably related to the structure heterogeneity and segregation. As a matter of fact, rhyolite and amphibolite are respectively (i) an igneous rock that exhibits a heterogeneous nodular structure composed of quartz and feldspath crystals, and (ii) a metamorphic rock with amphibole and plagioclase feldspars weakly foliated. The distribution of these heterogeneities differs from sample to sample and could explain the measured difference. Gneiss and quartz arenite are respectively (i) a metamorphic rock

with foliation and (ii) a sedimentary rock with micro-craking filled with quartz. These horizontal structures are randomly oriented into the samples and according to the Hashin-Shtrikman bounds (Brovelli and Cassiani, 2010), affect the measured permittivity. Relations between rock permittivity and bulk density are plotted in the Fig.2. The three following empirical laws are studied:

$$\epsilon^{'} = a_1^{\rho} \tag{1}$$

The equation 1 is given by Ulaby et al. (1990) for terrestrial rocks and by Olhoeft and Stangway (1975) for lunar materials, where $a_1 = 1.96$ and $a_1 = 1.93$, respectively;

$$\epsilon^{'} = (a_2 + a_3\rho)^2 \tag{2}$$

The equation 2 is given by Shutko (1982) for dry soil, where $a_2 = 1$ and $a_3 = 0.5$;

$$\epsilon^{'} = (a_4 + a_5\rho)^2 - a_6 \tag{3}$$

The equation 3 is given by Dobson et al. (1985) for soil having extremely low moisture content, where $a_4 = 1.01$, $a_5 = 0.44$ and $a_6 = 0.062$;

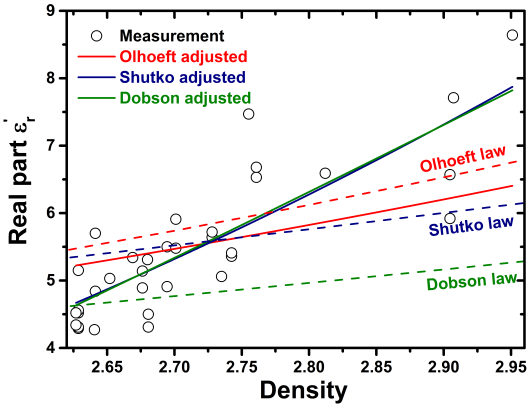

Figure 2: Real part of the permittivity as a function of the density according to Olhoeft, Shutko and Dobson laws (dashed lines) and then adjusted (solid lines).

As it can be seen on the Fig.2, none of the previous laws is adapted to the studied rocks. Thus, the parameters are adjusted to this specific application and give the following values : $a_1 = 1.88$, $a_2 = 3.1$, $a_3 = -2$, $a_4 = 3.1$, $a_5 = 0.89$ and $a_6 = 24.5$. The Olhoeft's law does not fit correctly the data (the correlation coefficient is R=0.64) while the best-adjusted laws are given by both Stuko and Dobson (R=0.83). However, the same conclusion established by Ulaby et al. (1990) can be drawn, meaning that the variation in the density accounts for about 50% of the observed variance in the dielectric constant ϵ' value. The remaining data scatter can be attributed to the mineral composition

of the rocks. Some of these observations were confirmed by Sengwa and Soni (2008) on dry minerals: at 10.1 GHz, they observed that both the density (of clay, fuller's earth, siliceous earth, tourmaline and magnesium rocks) and the chemical composition - and particularly the SiO_2, Al_2O_3 and FeO_3 oxides content - equally affect the measured ϵ'. As the previous authors concluded, no obvious relation between the density and the imagininary part of the permittivity can be established.

These assumptions would deserve a complementary study (i) by characterizing the chemical composition and the crystalline structure and (ii) by extending the frequency range of measurements.

3. Theoritical approach and application of models

3.1. Definition and presentation of the models

3.1.1. Definition of HMA density and compactness

HMA is considered as 4-phase mixture composed of binder, filler, aggregate and air. Density and compactness HMA have already been studied by Al-Qadi et al. (2010), Leng et al. (2011) for 3-phase mixture and by Fauchard et al. (2013, 2015) for 4-phase mixture. Here is a brief remind of these basic principles. Density ρ, weight content T, volume V and real part of the permittivity ϵ of each component are depicted in the Fig.3(a). The indexes b, f, a, and air refer respectively to binder, filler, aggregate and air. All densities and weight contents are provided by the road manufacturer for on site control, except the air void content that determines the mechanical objective of the road construction. In Europe, aggregates and filler densities are measured according to the NF-EN 18545 standard. The bitumen density is measured according to the NF-EN 15326+A1 standard. The HMA formulation is controlled (I) in laboratory, every year by an independent organism, and (ii) on site, by cores sampling every time a road is manufactured. Permittivity of each component are measured in laboratory. The related critical parameter to assess on newly-paved roads are (i) the density of the mix including air (namely bulk specific gravity) ρ_{HMAS} or (ii) the compactness C [2] of the HMA, related to each other by the following relation:

$$C = 1 - C_{air} = \frac{\rho_{HMAS}}{\rho_{HMAM}} \tag{4}$$

Where ρ_{HMAM} is the theoritical density of the HMA without air (namely maximum specific gravity).

It is the controlled parameter in France and other European countries.

All material contents are defined with respect to the total dry mass $m_s = m_a + m_b + m_f$. The weight content is simply $T_i = \frac{m_i}{m_s}$. The volumic fraction of the i^{th} component is defined as below:

$$C_i = C_a T_{i\neq a} \frac{\rho_a}{\rho_{i\neq a}} \tag{5}$$

And:

[2] Compactness can be expressed from 0 to 1 (unitless) or from 0 to 100 %.

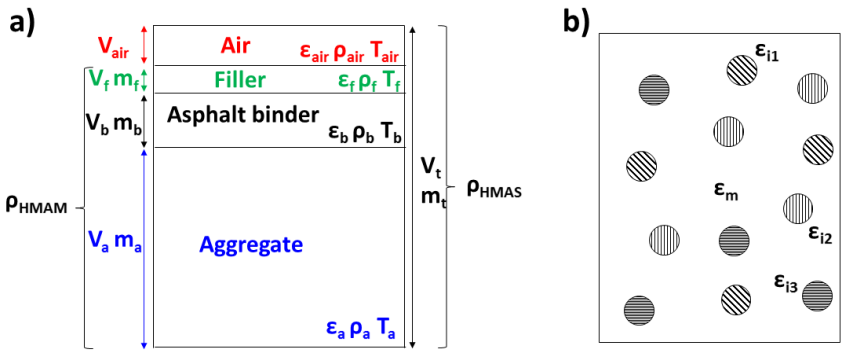

Figure 3: a) HMA representation and distribution of its components, and b), dielectric 4-phase mixture where the matrix permittivity ϵ_m can be either aggregate or binder.

$$C_a = \frac{C}{Z} \tag{6}$$

Where:

$$Z = 1 + \frac{\rho_a T_b}{\rho_b T_a} + \frac{\rho_a T_f}{\rho_f T_a} = 1 + C_{rb} + C_{rf} \tag{7}$$

3.1.2. Model assumptions

In this section, the basic concept of electromagnetic models are taken from Sihvola (1999), Sihvola and Kong (1988) and Parkhomenko (1967). HMA is assumed following two assumptions:

First, it is considered as a multiphase media composed of binder, filler, aggregate and air, where the permittivity and volumic fraction of each component average the effective permittivity of the media. This first model family is called the Power Law (PL) model which does not differenciate host component from the guests.

Second, the HMA (Fig.3(b)) is considered as several spherical inclusions immersed in a host matrix. In this work, the filler content is very low (about 1%) and the air is considered randomly distributed into the media. Hence, the host matrix can be either aggregate that presents the greater proportion in the mix or binder that encloses the remaining components. Under this assumption, the Unified Mixing Rules (UMR) can described the dielectric behaviour of the mix. Models acronym are detailed in table 2.

Both dielectric approaches are presented in the following section and the HMA compactness/density are calculated.

3.1.3. Power Law model

The PL model gives the HMA dielectric constant as a sum of each permittivity component weighted by their volumic concentration. It is defined according to the following formula:

$$\epsilon_{HMA}^{\alpha} = \sum_i C_i \epsilon_i^{\alpha} \tag{8}$$

The parameter α is known in the literature to have several values: when $\alpha = 1/2$, (8) gives the Complex Refractive Index Model, also called CRIM model or Birchak formula (Birchak et al., 1974). As explained by Sen et al. (1981), this assumption can be seen as a 3D-generalisation of the 1D-multilayered case of an EM field in normal incidence where the square root of the effective permittivity is the sum of the lineic concentration multiplied by the square root permittivity of each layer. If $\alpha = 1/3$, (8) is the Looyenga formula (Looyenga, 1965). Both cases $\alpha = 1$ and $\alpha = -1$ can be explained by considering a circuit capacitors, respectively (i) parrallel and (ii) series connected (Sihvola, 1999). Finally, for the limit $\alpha \to 0$, (8) is simply the Lichtenecker and Rother (1931) approximation given by:

$$ln(\epsilon_{HMA}) = \sum_i C_i ln(\epsilon_i) \tag{9}$$

(9) is obtained by taking into account the first order term of the Taylor series of the exponential function $e^{\alpha ln(\epsilon)}$.

By combining the equations (4-8), the HMA compactness and density are calculated by the following relations:

$$C = \frac{(\epsilon_{HMA}^{\alpha} - 1)Z}{\epsilon_a^{\alpha} + C_{rf}\epsilon_f^{\alpha} + C_{rb}\epsilon_b^{\alpha} - Z} \tag{10}$$

$$\rho_{HMAS} = \frac{(\epsilon_{HMA}^{\alpha} - 1)Z}{\epsilon_a^{\alpha} + C_{rf}\epsilon_f^{\alpha} + C_{rb}\epsilon_b^{\alpha} - Z}\rho_{HMAM} \tag{11}$$

3.1.4. Unified mixing rule formula

UMR allows writting the effective permittivity by considering a host matrix with guest inclusions (Sihvola, 1999; Sihvola and Kong, 1988).

$$\frac{\epsilon_{HMA} - \epsilon_m}{\epsilon_{HMA} + d_m} = \sum_i C_i \frac{\epsilon_i - \epsilon_m}{\epsilon_i + d_m} \tag{12}$$

Where ϵ_m is the permittivity of the host matrix m and $d_m = 2\epsilon_m + \nu(\epsilon_{HMA} - \epsilon_m)$.

After solving (12) by assuming that the matrix is the aggregate,

$$C = \frac{\frac{\epsilon_{HMA}-\epsilon_a}{\epsilon_{HMA}+d_a} - \frac{1-\epsilon_a}{1+d_a}}{\frac{1}{Z}C_{rb}\frac{\epsilon_b-\epsilon_a}{\epsilon_b+d_a} + \frac{1}{Z}C_{rf}\frac{\epsilon_f-\epsilon_a}{\epsilon_f+d_a} - \frac{1-\epsilon_a}{1+d_a}} \tag{13}$$

$$\rho_{HMAS} = \frac{\frac{\epsilon_{HMA}-\epsilon_a}{\epsilon_{HMA}+d_a} - \frac{1-\epsilon_a}{1+d_a}}{\frac{1}{Z}C_{rb}\frac{\epsilon_b-\epsilon_a}{\epsilon_b+d_a} + \frac{1}{Z}C_{rf}\frac{\epsilon_f-\epsilon_a}{\epsilon_f+d_a} - \frac{1-\epsilon_a}{1+d_a}}\rho_{HMAM} \tag{14}$$

Where $d_a = 2\epsilon_a + \nu(\epsilon_{HMA} - \epsilon_a)$.

After solving (12) by assuming that the matrix is the binder,

$$C = \frac{\frac{\epsilon_{HMA}-\epsilon_b}{\epsilon_{HMA}+d_b} - \frac{1-\epsilon_b}{1+d_b}}{\frac{1}{Z}\frac{\epsilon_a-\epsilon_b}{\epsilon_a+d_b} + \frac{1}{Z}C_{rf}\frac{\epsilon_f-\epsilon_b}{\epsilon_f+d_b} - \frac{1-\epsilon_b}{1+d_b}} \tag{15}$$

$$\rho_{HMAS} = \frac{\frac{\epsilon_{HMA}-\epsilon_b}{\epsilon_{HMA}+d_b} - \frac{1-\epsilon_b}{1+d_b}}{\frac{1}{Z}\frac{\epsilon_a-\epsilon_b}{\epsilon_a+d_b} + \frac{1}{Z}C_{rf}\frac{\epsilon_f-\epsilon_b}{\epsilon_f+d_b} - \frac{1-\epsilon_b}{1+d_b}}\rho_{HMAM} \tag{16}$$

Where $d_b = 2\epsilon_b + \nu(\epsilon_{HMA} - \epsilon_b)$.

The factor ν is a dimensionless parameter: $\nu = 0$ gives the Maxwell-Garnett rule also named Rayleigh model (Sihvola, 1999). $\nu = 2$ gives the Polder-Van Santen (Polder and Van Santen, 1946) formula or Böttcher formula (Böttcher et al., 1974) and $\nu = 3$ gives the Coherent potential approximation (Sen et al., 1981). This formula is valuable for 3D inclusions meaning that they are assumed to be spherical. However, inclusions can also be in 2D such as disk shaped. According to Wiener (1910) and Yaghjian (1980), the difference between both shapes is the factor $2\epsilon_m$ for 3D inclusions at the denominators which becomes ϵ_m for 2D inclusions.

3.2. Models application to laboratory HMA slabs

Lab experiments were conducted on two 40*60*8 cm slabs with a SFR system composed of the PNA described in section II and mono-static ultra wideband antenna of bandpass [1.4-6 GHz]. The tested slabs are mainly composed of basalt aggregates (0/10 mm) and the weight content, permittivity and density of each component are presented in the table 3. Binder and filler permittivities have been measured by means of cylindrical cavities. In order to analyze the behaviour of the models described in section 3.1, the density and compactness are calculated for every models in a theoritical HMA permittivity range of [1-7], corresponding to air void content ranging between 100% to 0%. This application is performed for the basalt slab described in the column 1 of table 3 (air void content of 13%) and is presented in the Fig.4(a).

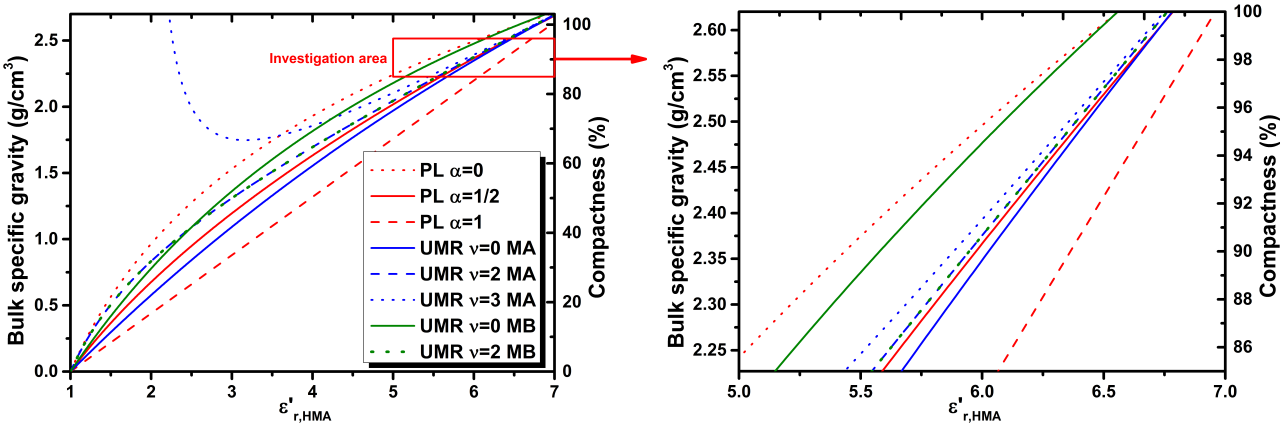

(a) HMA model behaviour from 100% to 0% air void content.

(b) HMA model behaviour in the investigation area.

Figure 4: Bulk specific gravity/compactness as a function of the real part of HMA permittivity (87% basalt slab): the red lines refer to the Power Law model, the blue lines to the Unified Mixing Rule with aggregate matrix and the green lines to Unified Mixing Rule with binder matrix.

The Fig.4(a) shows PL and UMR models tested with various parameter values: (i) $\alpha = [0; 1/2; 1]$ and (ii) $\nu = [0; 2; 3]$ for an aggregate matrix (MA) and $\nu = [0; 2]$ for a binder matrix (MB), respectively.

Generally speaking, four of these models give relatively similar calculated compactness. Indeed CRIM (PL $\alpha = 1/2$), Rayleigh (UMR $\nu = 0$ MA) and Böttcher (UMR $\nu = 2$ MA and MB) models seem to be close especially as

soon as the permittivity is near from the investigated area [85% $\leq C \leq$ 96%]. A noticeable crossover point can be observed for a permittivity equal to 2.5 (i.e. binder permittivity) for UMR family model with binder matrix. Above and below this crossover point, models behave differently from each other, which is the first visible consequence of the chosen matrix. The choice of the matrix does not have any effect concerning the Böttcher model (UMR $\nu = 2$): as it is seen on the Fig.4(a) green dot line and blue dashed line are exactly superimposed whereas blue line and green line (Rayleigh model, UMR $\nu = 0$) are far from each other. This can be easily explained by looking at the denominator in (8). Böttcher model gives more importance to the HMA permittivity ($3\epsilon_{HMA}$) while Rayleigh gives to the matrix permittivity ($\epsilon_{HMA} + 2\epsilon_a$). A basic calculation proves that the compactness of UMR $\nu = 2$ MA and UMR $\nu = 2$ MB are strictly equal. Coherent potential approximation (UMR $\nu = 3$ MA) for an aggregate matrix (blue dot line) exhibits a huge deviation of the calculated compactness for the HMA permittivity between 1 to 4. This deviation is explained by Sihvola (1999) as the percolation point who pictures a huge change of the model behaviour for a small variation of the permittivity. In the Fig.4(a), the blue dot line below this percolation point is not represented. PL family shows a significant difference in the calculated compactness for a given value of α. The CRIM model (PL $\alpha = 1/2$) widely used by Fauchard et al. (2015) gives closest results with the Böttcher (UMR $\nu = 2$ MA and MB) and Rayleigh (UMR $\nu = 0$ MA).

The target air void content in civil engineering is usually comprised between 15% (such low compactness is usually used for porous asphalt) and 4%. The Fig.4(b) is a zoom of the Fig.4(a) in the investigated compactness area. As it is seen, the PL $\alpha = 1/2$ and the Böttcher (UMR $\nu = 2$ MA and MB) models are very closed from each other. The Coherent potential approximation (UMR $\nu = 3$ MA) and Rayleigh (UMR $\nu = 0$ MA) models have a slight deviation from both sides of the three previous models. However, Rayleigh (UMR $\nu = 0$ MB), Lichetenecker-Rother (PL $\alpha = 0$) and Silberstein (PL $\alpha = 1$) models exhibit a huge deviation from the five other models. The highest the compactness, the closest is the HMA permittivity. For the studied slab with $C = 87\%$, the difference of the calculated compactness can be expected to be larger than the slab with $C = 95\%$.

3.3. Models application to laboratory HMA slabs

In this section, the HMA permittivity is measured with a SFR system. The experimental system and the theoritical background of the HMA permittivity measurement have already been well described by Fauchard et al. (2015). In this work, the HMA permittivity ϵ_{HMA} is assessed thanks to the two-way travel time Δt of the EM wave into the slab and its thickness e according to the equation: $\epsilon_{HMA} = (\frac{c\Delta t}{2e})^2$. The SFR permittivity measurements on the slab surfaces were performed every 5 cm along the x-axis, and every 1 cm along y-axis. In order to avoid the edge effects, a 40 cm*20 cm smaller surface is taken into account. Then, the compactness and the density of the slabs are calculated with the models PL $\alpha = 1/2$ and UMR $\nu = [0; 2]$, MA and MB (with 10-11 and 13-16, respectively). UMR with 2D inclusions (disk shaped) was also tested on the slabs, but systematic offsets were observed meaning that the disk shape inclusions are not adapted for this material. This case is not presented here. The compactness and the density obtained with a gamma bench is considered as the reference value (NF EN 12697-7, 2003). The result of the measurement

is represented as a color map along x and y axis. The color scale represents the assessed compactness. The whole experiment was carried out on 4 slabs of various target air void contents (87%, 90%, 92% and 95%) both on top and bottom surfaces. In this paper, only the top surface 87% and 95% slabs results are presented in the Fig.5 and 6.

3.4. In-lab results interpretation and discussion

First of all, a design flaw called rutting effect can be observed on the slabs especially for the 95% compactness slab. This is observable by a lower calculated compactness along the y-axis following two bands corresponding to the passage of the wheels during the compaction process. However this rutting effect is not observed on the gamma bench measurement, meaning that the slabs were implemented homogeneously. Hence, the explanation can only be attributed to the two-way travel time measured with the SFR that was already observed and explained by Fauchard et al. (2013). The table 4 summarizes the average compactness and the average density of each slabs according to the reference value (gamme bench) and the studied models. The compactness of the 87% designed slab is exactly as expected (87.2%). Withal, gamma bench measurement on the 95% designed slab exhibits a compactness of 92.6% due to a manufacturing constraint. The values obtained by gamma bench will be now considered as the true compactness. In the present results, for both slabs and every models, the calculated compactness is close to the reference value, except for the Rayleigh model (UMR $\nu = 0$) with binder matrix. Indeed, the UMR $\nu = 0$ MB overestimates the compactness from 3 to 6% depending on the selected slab and exhibits a systematic shift compared to the other models. However, the UMR $\nu = 0$ MA calculation gives excellent results for both slabs - particularly for the 87% slab (from 0.003 to the reference value) - which suggests that aggregate matrix is the appropriate choice.

The Böttcher model UMR $\nu = 2$ MA and MB are strictly identical and as explained previously, a basic calculation of both models proves that 13-14 are equal to 15-16. In that case, the matrix nature does not affect the calculation. UMR $\nu = 2$ MA and MB point out excellent results as well, with a best-calculated compactness for the 95% slab (from 0.004 to the reference value).

As described earlier, the PL $\alpha = 1/2$ model is a part of the group that exhibits excellent results. Consequently, CRIM model is very close to the gamma bench compactness (from 0.007 to 0.011). In that formalism, the PL does not distinguish the host matrix from guest inclusions. Previous works (Fauchard et al., 2015) shown that PL $\alpha = 1/2$ is a relevant model for HMA compactness assessment. As UMR ν=[0,2] MA are relatively similar to the reference value and the PL $\alpha = 1/2$, it could suggest that aggregate as host matrix is a valid choice.

For the present lab experiment, the slabs were manufactured with basalt rock extracted from a single vein and controlled by means of cylindrical cavities. This leads to the assumption that the aggregate permittivity is constant into the whole slab, tacking into account the standard deviation of 2%. Following this consideration, the PL $\alpha = 1/2$ and the UMR ν=[0,2] MA models might be considered as equivalent for the lab compactness/density assessment.

Al-Qadi et al. (2010) have shown for their on-site application that the Rayleigh model with binder matrix gave closest results from the reference value than the CRIM and Böttcher models. In another work, Leng et al. (2011) concluded that the Böttcher model was the most accurate for their on-site case study. Finally, Fauchard et al. (2015)

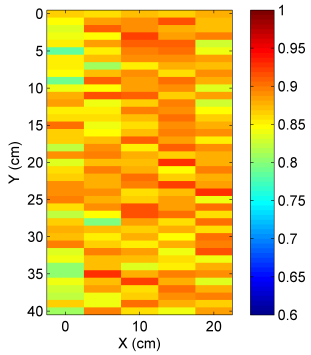

(a) Gamma bench compactness: $C = 0.872 \pm 0.027$

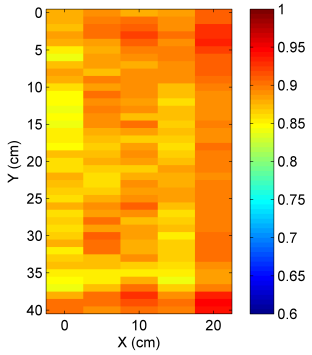

(b) PL $\alpha = 1/2$: $C = 0.883 \pm 0.020$

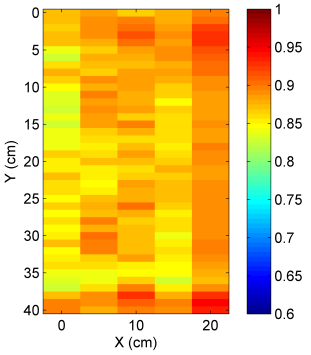

(c) UMR $\nu = 0$ MA: $C = 0.875 \pm 0.022$

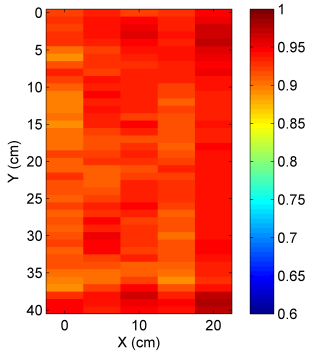

(d) UMR $\nu = 0$ MB: $C = 0.929 \pm 0.017$

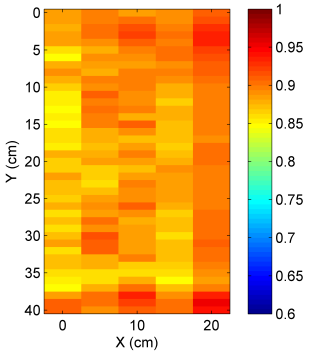

(e) UMR $\nu = 2$ MA and MB: $C = 0.888 \pm 0.019$

Figure 5: Assessed compactness on the 87% slab by means of SFR system obtained with a) the reference gamma bench system, b) the CRIM model (PL $\alpha = 1/2$), c) the Rayleigh model with aggregate matrix ([UMR $\nu = 0$ MA), d) the Rayleigh model with binder matrix ([UMR $\nu = 0$ MB) and e) the Böttcher model with aggregate and binder matrix (UMR $\nu = 2$ MA and MB).

carried out on-site compactness assessment by using PL $\alpha = 1/2$ in great accordance with standard nuclear and core testing. For all of these approaches, the aggregate permittivity was back-computed according to density cali-

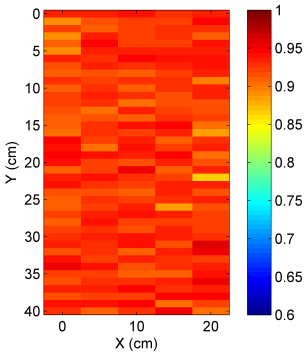

(a) Gamma bench compactness: $C = 0.926 \pm 0.014$

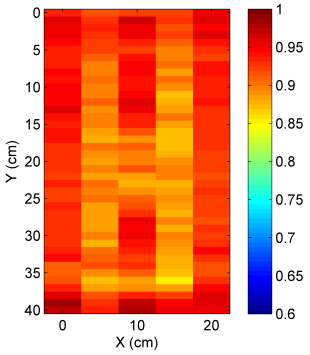

(b) PL $\alpha = 1/2$: $C = 0.919 \pm 0.026$

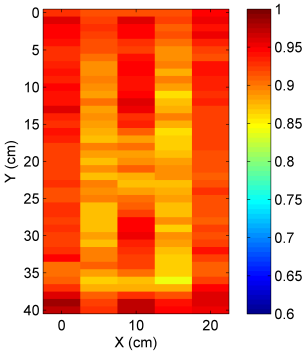

(c) UMR $\nu = 0$ MA: $C = 0.913 \pm 0.028$

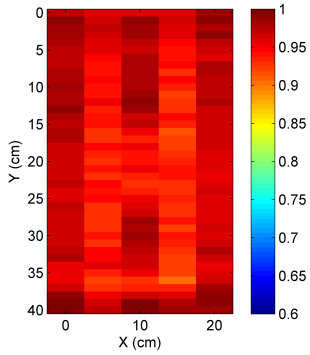

(d) UMR $\nu = 0$ MB: $C = 0.958 \pm 0.021$

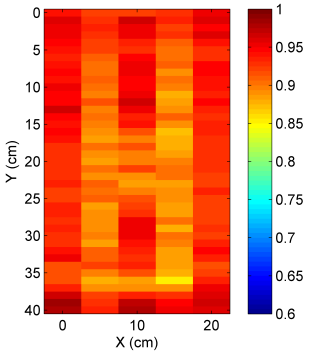

(e) UMR $\nu = 2$ MA and MB: $C = 0.922 \pm 0.025$

Figure 6: Assessed compactness on the 95% slab by means of SFR system obtained with a) the reference gamma bench system, b) the CRIM model (PL $\alpha = 1/2$), c) the Rayleigh model with aggregate matrix ([UMR $\nu = 0$ MA), d) the Rayleigh model with binder matrix ([UMR $\nu = 0$ MB) and e) the Böttcher model with aggregate and binder matrix (UMR $\nu = 2$ MA and MB).

bration by core drilling. Due to the multiple parameters which could influence the accuracy of the HMA measured permittivity, the same conclusion can be drawn, i.e. the three aforementionned models can be usable for the *in-situ*

compactness/density assessment.

4. Conclusion

The objective of this work has been to characterize the dielectric properties of rocks used in pavement assessment in order to calculate the HMA compactness from electromagnetic mixing models. The dielectric investigation has shown that the studied rocks can be considered either as near perfect dielectric or low loss dielectric with a real permittivity ranges from 4 to 9. Application of Olhoeft and Stangway (1975), Shutko (1982) and Dobson et al. (1985) fitting pointed out that the real permittivity is dependent upon the density and the chemical composition of the rock. Further studies need to be performed concerning the structural and chemical composition of the rocks in order to support these assumptions. It could be of great interest to carry out the dielectric behaviour on a wider frequency range so that the behaviour of dry rocks at high frequencies could be better understood. The comparison of the two electromagnetic mixing model families recently used for HMA assessment has been performed on laboratory slabs whose the permittivity of each component was measured by means of cylindrical cavities (binder, filler and aggregate). Slabs were controlled by gamma bench measurement as standard for comparison with applied models. This investigation highlights that the PL $\alpha = 1/2$ (CRIM), UMR ν=0 MA (Rayleigh) and UMR ν=2 MA (Böttcher) models gave excellent results in correlation with the reference compactness. Thereby, it was concluded that choosing aggregate as matrix for the UMR family is more appropriate than binder. In consideration of the uncertainties of radar measurement or permittivity measurement for both on site and lab experiments, the three models i.e. PL $\alpha = 1/2$ (CRIM), UMR ν=0 MA (Rayleigh) and UMR ν=2 MA (Böttcher) can be considered as equivalent. These models deserve to be applied on different slab natures in order to study their deviation and further *in-situ* investigations should be undertaken for validation.

ACKNOWLEDGEMENTS

A sincere thanks goes to the reviewers for their relevant comments to improve the manuscript. The authors would like to thank Cyril Ledun (Cerema) and Henri Mauduit (Université de Rouen) for their help to the permittivity measurements. They also express their gratitude to Aminata Diouf (INSA de Rouen) for her precious help. This study would not have been possible without the financial support of USIRF (Union des syndicats des industries routières françaises and Région Haute-Normandie). We are very grateful to the COST Action TU1208 "Civil Engineering Applications of Ground Penetrating Radar".

REFERENCES

Al-Qadi, I., Lahouar, S., 2004. Use of gpr for thickness measurement and quality control of flexible pavements (with discussion). Journal of the Association of Asphalt Paving Technologists 73.

Al-Qadi, I.L., Leng, Z., Lahouar, S., Baek, J., 2010. In-place hot-mix asphalt density estimation using ground-penetrating radar. Transportation Research Record: Journal of the Transportation Research Board 2152, 19–27.

ASTM D2950 / D2950M, 2011. Standard test method for density of bituminous concrete in place by nuclear methods .

ASTM D6938 - 10, 2010. Standard test method for in place density and water content of soil and soil aggregate by nuclear methods (shallow depth) .

290 Benedetto, A., 2010. Water content evaluation in unsaturated soil using gpr signal analysis in the frequency domain. Journal of Applied Geophysics
291 71, 26–35.
292 Benedetto, A., Tosti, F., 2013. Inferring Bearing Ratio of Unbound Materials from Dielectric Properties Using GPR: The Case of Runaway Safety
293 Areas. chapter 113. pp. 1336–1347. http://ascelibrary.org/doi/pdf/10.1061/9780784413005.113.
294 Birchak, J.R., Gardner, C.G., Hipp, J.E., Victor, J.M., 1974. High dielectric constant microwave probes for sensing soil moisture. Proceedings of
295 the IEEE 62, 93–98.
296 Bona, N., Ortenzi, A., Capaccioli, S., 2002. Advances in understanding the relationship between rock wettability and high-frequency dielectric
297 response. Journal of Petroleum Science and Engineering 33, 87–99.
298 Böttcher, C., Van Belle, O., Bordewijk, P., Rip, A., Yue, D.D., 1974. Theory of electric polarization. Journal of The Electrochemical Society 121,
299 211C–211C.
300 Brovelli, A., Cassiani, G., 2010. A combination of the hashin-shtrikman bounds aimed at modelling electrical conductivity and permittivity of
301 variably saturated porous media. Geophysical Journal International 180, 225–237.
302 Campbell, M.J., Ulrichs, J., 1969. Electrical properties of rocks and their significance for lunar radar observations. J. Geophys. Res. 74, 5867–5881.
303 Chelidze, T.L., Gueguen, Y., 1999. Electrical spectroscopy of porous rocks: a reviewi. theoretical models. Geophysical Journal International 137,
304 1–15. http://gji.oxfordjournals.org/content/137/1/1.full.pdf+html.
305 Chelidze, T.L., Gueguen, Y., Ruffet, C., 1999. Electrical spectroscopy of porous rocks: a reviewii. experimental results and interpretation. Geo-
306 physical Journal International 137, 16–34. http://gji.oxfordjournals.org/content/137/1/16.full.pdf+html.
307 Dobson, M., Ulaby, F., Hallikainen, M., El-Rayes, M., 1985. Microwave dielectric behavior of wet soil-part ii: Dielectric mixing models. Geo-
308 science and Remote Sensing, IEEE Transactions on GE-23, 35–46.
309 Fauchard, C., Beaucamp, B., Laguerre, L., 2015. Non-destructive assessment of hot mix asphalt compaction/ density with a step-frequency radar:
310 case study on a newly paved road. Near Surface Geophysics 13, 289–297.
311 Fauchard, C., Li, B., Laguerre, L., Hritier, B., Benjelloun, N., Kadi, M., 2013. Determination of the compaction of hot mix asphalt using high-
312 frequency electromagnetic methods. NDT & E International 60, 40–51.
313 Gomaa, M.M., Elsayed, R., 2009. Thermal effect of magma intrusion on the electrical properties of magnetic rocks from hammamat sediments,
314 Cairo, Egypt. Geophysical Prospecting 57, 141–149.
315 Hallikainen, M., Ulaby, F., Dobson, M., El-Rayes, M., Wu, L.K., 1985. Microwave dielectric behavior of wet soil-part 1: Empirical models and
316 experimental observations. Geoscience and Remote Sensing, IEEE Transactions on GE-23, 25–34.
317 Hasar, U., 2009. Non-destructive testing of hardened cement specimens at microwave frequencies using a simple free-space method. NDT & E
318 International 42, 550–557.
319 Kaden, H., Kniger, F., Strmme, M., Niklasson, G.A., Emmerich, K., 2013. Low-frequency dielectric properties of three bentonites at different
320 adsorbed water states. Journal of Colloid and Interface Science 411, 16 – 26.
321 Leng, Z., Al-Qadi, I.L., Lahouar, S., 2011. Development and validation for in situ asphalt mixture density prediction models. NDT & E International
322 44, 369–375.
323 Lesmes, D.P., Morgan, F.D., 2001. Dielectric spectroscopy of sedimentary rocks. Journal of Geophysical Research: Solid Earth 106, 13329–13346.
324 Li, S., Akyel, C., Bosisio, R., 1981. Precise calculations and measurements on the complex dielectric constant of lossy materials using tm010
325 cavity perturbation techniques. IEEE Transactions on Microwave Theory and Techniques 29, 1041 – 1048.
326 Lichtenecker, K., Rother, K., 1931. Die herleitung des logarithmischen mischungsgesetzes aus allgemeinen prinzipien der stationiren strmung.
327 phys. Z 32, 255–260.
328 Looyenga, H., 1965. Dielectric constants of heterogeneous mixtures. Physica 31, 401–406.
329 Lopatin, V.V., Martemyanov, S.M., 2012. Investigation of the dielectric properties of oil shale. Russian Physics Journal 55, 35–39.
330 Maierhofer, C., Wöstmann, J., 1998. Investigation of dielectric properties of brick materials as a function of moisture and salt content using a
331 microwave impulse technique at very high frequencies. NDT & E International 31, 259–263.
332 NF EN 12697-6, 2012. Mélanges bitumineux - méthodes d'essai pour mélange hydrocarboné chaud - partie 6 : détermination de la masse

volumique apparente des éprouvettes bitumineuses .

NF EN 12697-7, 2003. Mélanges bitumineux - méthodes d'essai pour mélange hydrocarboné chaud - partie 7 : détermination de la masse volumique apparente des éprouvettes bitumineuses par les rayons gamma .

Olhoeft, G.R., Stangway, D.W., 1975. Dielctric properties of the first 100 meters of the moon. Eart Planet Sci. Lett. 24, 394–404.

Parkhomenko, E.I., 1967. Electrical Properties of Rocks. Springer US.

Polder, D., Van Santen, J., 1946. The effective permeability of mixtures of solids. Physica 12, 257–271.

Robert, A., 1998. Dielectric permittivity of concrete between 50 mhz and 1 ghz and gpr measurements for building materials evaluation. Journal of Applied Geophysics 40, 89–94.

Saint-Amant, M., Strangway, D., 1970. Dielectric properties of dry, geological materials. Geophysics 35, 624–645.

Saltas, V., Vallianatos, F., Triantis, D., 2008. Dielectric properties of non-swelling bentonite: The effect of temperature and water saturation. Journal of Non-Crystalline Solids 354, 5533 – 5541.

Sen, P.N., Scala, C., Cohen, M.H., 1981. A self-similar model for sedimentary rocks with application to the dielectric constant of fused glass beads. Geophysics 46, 781–795. http://dx.doi.org/10.1190/1.1441215.

Sengwa, R.J., Soni, A., 2008. Dielectric properties of some minerals of western Rajasthan. Indian Journal of Radio & Space Physics 37, 57–63.

Shutko, A.M., 1982. Microwave radiometry of lands under natural and artificial moistening. Geoscience and Remote Sensing, IEEE Transactions on GE-20, 18–26.

Sihvola, A., Kong, J.A., 1988. Effective permittivity of dielectric mixtures. Geoscience and Remote Sensing, IEEE Transactions on 26, 420–429.

Sihvola, A.H., 1999. Electromagnetic mixing formulas and applications. The Institute of Electrical Engineers, London.

Tong, M., Tao, H., 2008. Permeability estimating from complex resistivity measurement of shaly sand reservoir. Geophysical Journal International 173, 733–739.

Ulaby, F., Bengal, T., Dobson, M., East, J., Garvin, J., Evans, D., 1990. Microwave dielectric properties of dry rocks. Geoscience and Remote Sensing, IEEE Transactions on 28, 325 –336.

Wiener, O., 1910. Zur theorie der refraktionskonstanten, berichte über die verhandlungen der königlich-sächsischen gesellschaft der wisseschaften zu leipzig. Math.-phys. Klasse 62, 256–277.

Yaghjian, A.D., 1980. Electric dyadic green's functions in the source region. Proceedings of the IEEE 68, 248–263.

Table 1: First column: the rock number (x-axis in Fig.1(a), 1(b) and 1(c)), the name, the measurement date (2013 and 2015), the quarry and the rock feature - subsequent columns: real and imaginary part of the permittivity measured at 0.57 GHz, 1 GHz, 1.7 GHz, 1.15 GHz, 2.63 GHz and 4.13 GHz in cylindrical cavities, corresponding loss tangent tanδ and density ρ.

Rock number - nature (quarry, date, feature)	$\epsilon_r^{'}$	$\epsilon_r^{''}$	tanδ	ρ
1a - Sandstone quartzite (Montebourg, 2015)	4.27±0.16	0.07±0.02	0.017±0.003	2.641
1b - Sandstone quartzite (Montebourg, 2013)	4.52±0.05	0.03±0.02	0.006±0.005	2.641
2 - Quartzite (Vignats, 2015, pink)	4.29±0.16	0.01±0.01	0.003±0.002	2.577
3a - Quartzite (Vignats, 2015, white)	4.31±0.14	0.03±0.02	0.007±0.005	2.629
3b - Quartzite (Vignats, 2013, white)	4.56±0.13	0.03±0.02	0.008±0.005	2.629
4a - Quartzite (Barenton, 2015)	4.31±0.17	0.02±0.01	0.004±0.003	2.681
4b - Quartzite (Barenton, 2013)	4.50±0.10	0.05±0.04	0.010±0.008	2.681
5a - Sandstone (Challoué, 2015)	4.34±0.13	0.01±0.01	0.003±0.002	2.623
5b - Sandstone (Challoué, 2013)	4.52±0.05	0.03±0.02	0.006±0.005	2.623
6a - Rhyolite (Averton Mayenne, 2015)	4.84±0.23	0.06±0.02	0.039±0.032	2.641
6b - Rhyolite (Averton Mayenne, 2013)	5.70±0.09	0.14±0.11	0.025±0.019	2.641
7a - Sandstone (Muneville-Le-Bingard, 2015)	4.89±0.06	0.10±0.07	0.019±0.014	2.676
7b - Sandstone (Muneville-Le-Bingard, 2013)	5.14±0.04	0.25±0.12	0.048±0.024	2.676
8a - Gneiss (Tinchebray, 2015)	4.91±0.16	0.01±0.01	0.002±0.001	2.695
8b - Gneiss (Tinchebray, 2013)	5.50±0.09	0.06±0.05	0.011±0.009	2.695
9 - Granite (Bonottières, 2015)	5.03±0.18	0.05±0.05	0.011±0.012	2.652
10 - Granite (Mouzière, 2015, microcrystalline)	5.06±0.18	0.09±0.06	0.016±0.012	2.735
11 - Quartzite (Vignats, 2015, red)	5.15±0.07	0.11±0.08	0.022±0.015	2.534
12 - Diorite (Noubleau, 2015, large grained)	5.31±0.26	0.04±0.03	0.008±0.005	2.680
13 - Granite (Gouraudière 2015, fine grained)	5.34±0.13	0.11±0.08	0.021±0.015	2.669
14a - Weathered granite (Ferrières, 2015)	5.36±0.08	0.03±0.01	0.005±0.003	2.742
14b - Weathered granite (Ferrières 2013)	5.41±0.07	0.08±0.06	0.015±0.011	2.742
15a - Quartz arenite (Roche Blain, 2015)	5.48±0.09	0.13±0.08	0.023±0.014	2.701
15b - Quartz arenite (Roche Blain, 2013)	5.91±0.04	0.22±0.17	0.037±0.029	2.701
16a - Hornfels (Saint-Honorine-Plafond, 2015)	5.64±0.11	0.04±0.02	0.007±0.004	2.728
16b - Hornfels (Saint-Honorine-Plafond, 2013)	5.72±0.15	0.1±0.06	0.017±0.012	2.728
17 - Limestone (Caen, 2015)	5.73±0.07	0.03±0.02	0.005±0.003	2.230
18 - Basalt (Python de la Fournaise, 2015)	5.82±0.07	0.31±0.12	0.053±0.021	2.094
19a - Amphibolite (Arvieux, 2015)	5.92±0.12	0.03±0.02	0.006±0.004	2.905
19b - Amphibolite (Arvieux, 2013)	6.57±0.25	0.07±0.05	0.010±0.008	2.905
20a - Gneissic sandstone (Vaubadon, 2015)	6.53±0.08	0.12±0.07	0.018±0.012	2.761
20b - Gneissic sandstone (Vaubadon, 2013)	6.68±0.09	0.18±0.14	0.028±0.021	2.761
21 - Diorite (Gouraudière, 2015, microcrystalline)	6.59±0.23	0.11±0.05	0.017±0.008	2.812
22 - Limestone (North region, 2013)	7.47±0.11	0.11±0.09	0.020±0.010	2.755
23 - Basalt (Rhône-Alpes region)	7.71±0.18	0.13±0.05	0.017±0.0050	2.907
24 - Diorite (Noubleau, 2015, medium grained)	8.64±0.16	0.18±0.09	0.021±0.011	2.951

Table 2: Models description

Acronym	Name (Authors)	Family	Parameter
PL $\alpha = 0$	Lichtenecker-Rother formula or logarithmyc law	Power law model	$\alpha = 0$
PL $\alpha = 1/3$	Looyenga formula	Power Law model	$\alpha = 1/3$
PL $\alpha = 1/2$	CRIM model or Birchak	Power Law model	$\alpha = 1/2$
PL $\alpha = 1$	Silberstein formula or linear law	Power Law model	$\alpha = 1$
UMR $\nu = 0$	Rayleigh model or Maxwell Garnett rule	Unified Mixing Rule 3D	$\nu = 0$
UMR $\nu = 2$	Böttcher model or Polder-van Santen	Unified Mixing Rule 3D	$\nu = 2$
UMR $\nu = 3$	Coherent potential approximation	Unified Mixing Rule 3D	$\nu = 3$

Table 3: Mix design of the studied HMA slabs

Aggregates	Basalt (0/10)	Basalt (0/10)
Designed compaction	0.87	0.95
T_a	0.927	0.932
T_b	0.056	0.058
T_f	0.017	0.01
ϵ_a	(7.71±0.20)-j(0.13±0.08)	(7.71±0.20)-j(0.13±0.08)
ϵ_b	(2.50±0.02)-j(0.003±0.002)	(2.50±0.02)-j(0.003±0.002)
ϵ_f	(7.2±0.02)-j(0.01±0.005)	(7.2±0.02)-j(0.01±0.005)
ρ_a (g/cm^3)	2.890	2.890
ρ_b (g/cm^3)	1.030	1.030
ρ_f (g/cm^3)	2.635	2.635

Table 4: Compactness (C) and density (ρ) results on HMA slabs designed for an air void content of 13% and 5%. In red color, the reference gamma bench (γ) measurement. Subsequent columns: PL model for $\alpha = 1/2$ and UMR models for $\nu = 0$ (Rayleigh) and $\nu = 2$ (Böttcher), both for aggregate matrix (MA) and binder matrix (MB).

Slabs	Gamma bench γ	PL $\alpha = 1/2$	UMR $\nu = 0$ MA	UMR $\nu = 0$ MB	UMR $\nu = 2$ MA	UMR $\nu = 2$ MB
$C_{87\%}$	0.872±0.027	0.883±0.020	0.875±0.022	0.929±0.017	0.888±0.019	0.888±0.019
$\rho_{87\%}$	2.285±0.071	2.315±0.053	2.292±0.057	2.434±0.043	2.325±0.051	2.325±0.051
$C_{95\%}$	0.926±0.014	0.919±0.026	0.913±0.028	0.958±0.021	0.922±0.025	0.922±0.025
$\rho_{95\%}$	2.421±0.036	2.398±0.041	2.386±0.073	2.504±0.054	2.410±0.066	2.410±0.066